Geophysical Research Letters

RESEARCH LETTER
10.1029/2018GL077527

Key Points:
- Intrathermocline eddies were observed within the thermocline of a large anticyclonic loop current eddy
- They are characterized by weak stratification and low Ertel potential vorticity
- The observation of three ITEs in a single transect suggests that they could be abundant

Correspondence to:
T. Meunier,
thomas.meunier@ifremer.fr

Citation:
Meunier, T., Tenreiro, M., Pallàs-Sanz, E., Ochoa, J., Ruiz-Angulo, A., Portela, E., et al. (2018). Intrathermocline eddies embedded within an anticyclonic vortex ring. *Geophysical Research Letters*, *45*, 7624–7633. https://doi.org/10.1029/2018GL077527

Received 9 FEB 2018
Accepted 3 MAY 2018
Accepted article online 11 MAY 2018
Published online 1 AUG 2018

Intrathermocline Eddies Embedded Within an Anticyclonic Vortex Ring

Thomas Meunier[1], M. Tenreiro[1], Enric Pallàs-Sanz[1], Jose Ochoa[1], Angel Ruiz-Angulo[2], Esther Portela[1], Simò Cusí[1], Pierre Damien[1], and Xavier Carton[3]

[1]Departamento de Oceanografía, CICESE, Ensenada, Mexico, [2]Centro de Ciencias de la Atmósfera, UNAM, Mexico City, Mexico, [3]Laboratoire d'Océanographie Physique et Spatiale, IUEM, Plouzané, France

Abstract High-resolution hydrographic measurements reveal the presence of three intrathermocline eddies (ITEs) embedded within a loop current eddy. ITEs are lenticular bodies of nearly homogeneous water, which contrasts with the well-stratified surrounding water. Their radii and thickness ranged between 19–32 km and 150–250 m. Negative relative vorticity within their cores (down to −0.85 times the Coriolis frequency), along with a large negative stratification anomaly, results in low Ertel potential vorticity and intense negative Ertel potential vorticity anomalies. Vortex stretching and relative vorticity have comparable contributions to potential vorticity anomaly, resulting in Burger numbers of order unity. The similarity of thermohaline properties within the ITE's cores and the surrounding loop current eddy water suggests that these ITEs likely form by intense mixing events followed by Rossby adjustment.

Plain Language Summary Small oceanic interior vortices, named *intrathermocline eddies*, were observed for the first time in the Gulf of Mexico using autonomous underwater gliders. These small eddies had the particularity to be embedded below a large and energetic anticyclonic eddy, which detached from the loop current 5 months before the survey. The physical properties of these structures are described, and their formation mechanisms, as well as potential impact on the redistribution of heat and salt in the Gulf of Mexico, are discussed.

1. Introduction

Intrathermocline eddies (ITEs; Dugan et al., 1982), also known as *submesoscale coherent vortices* (McWilliams, 1985) are common features of the ocean interior. They typically are anticyclonic structures, consisting of a lenticular body of nearly homogeneous water splitting the pycnocline. Their thermohaline properties sharply contrast with the surroundings (Kostianoy & Belkin, 1989). Their velocity field is characterized by a deep maximum of azimuthal velocity presenting an azimuthal symmetry (Thomas, 2008). They are particularly abundant in the vicinity of major intermediate water outflows such as the Mediterranean (Hebert, 1988), Persian Gulf (L'Hégaret et al., 2016), or Red Sea (Shapiro & Meschanov, 1991) outflows, but ITEs were also extensively observed in various oceanic basins, marginal seas, or current systems, such as the Arctic Ocean (Kostianoy & Belkin, 1989), Beaufort sea (D'Asaro, 1988a), Mediterranean Sea (Brenner, 1989; Damien et al., 2017), Bay of Biscay (Pingree & Le Cann, 1992), Tasman Sea (Baird & Ridgway, 2012), Sargasso sea (Dugan et al., 1982), Labrador sea (Lilly & Rhines, 2002), California Under Current (Collins et al., 2013), Peru-Chile Under Current (Thomsen et al., 2016), and in the Bay of Bengal (Gordon et al., 2017).

Various formation mechanisms were proposed, including baroclinic instability of undercurrents (Jungclaus, 1999), lateral frictional processes near capes or promontories (D'Asaro, 1988b; Molemaker et al., 2015), diapycnal mixing whether by bottom friction (McWilliams, 1985) or locally intensified internal wave breaking (Lelong & Sundermeyer, 2005; Stuart et al., 2011), winter convection (Testor & Gascard, 2003), or subduction along frontal zones (Ou & Gordon, 2002; Thomas, 2008). They are associated with low values of Ertel potential vorticity (PV) and Brunt-Väisälä frequency, and fairly high Rossby numbers. They are known to have a particularly long lifetime (up to 2 years for meddies; Armi et al., 1989), which allows them to carry water mass properties far away from their formation zones, slowly diffusing their heat and salt content and biogeochemical properties to the surrounding waters.

Because of their intrathermocline localization, ITEs are often described as isolated structures. However, on rare occasions, they were reported to be embedded or trapped within larger-scale eddies (Baird & Ridgway, 2012; Hallock et al., 1981; Gordon et al., 2002). The present manuscript reports recent in situ glider observations within the Gulf of Mexico (GoM) of three ITEs embedded within the main thermocline of a loop current eddy (LCE).

LCEs are large and energetic near-surface intensified anticyclonic vortex rings detaching sporadically from the loop current (Elliott, 1982; Ichiye, 1959; Vukovich, 1995). They drift westward through the GoM (Glenn & Ebbesmeyer, 1993; Johnson et al., 1992), carrying warm and salty subtropical underwater (SUW; (Hernández-Guerra & Joyce, 2000; Wüst, 1964)). LCE Poseidon (Meunier et al., 2018), in which the ITEs were observed, was a large (300 km in diameter) structure with particularly large temperature and salinity anomalies (up to 9.7° and 1.22 psu) resulting in an almost homogeneous core of warm and salty water surrounded above and below by well stratified thermocline water. The maximum velocity ranged from 0.8 to 1.5 m/s in subsurface at the eddy's periphery, at about 150 km from its center.

In this paper, the thermohaline and dynamical properties of these ITEs are studied through an examination of the fine-scale hydrographic data collected through Poseidon. Their formation process, as well as their possible impact on the diffusion of SUW in the GoM are also discussed.

2. Data and Methods

The data were collected during a full cross-transect through LCE Poseidon (Figure 1a) using an autonomous underwater vehicle (glider) equipped with an unpumped *Seabird CT-Sail*® CTD probe. It sampled the water column from the surface down to 1,000 m at average horizontal and vertical speeds of 0.15 m/s and a sampling rate of 0.15 Hz. The resulting average horizontal and vertical resolutions were of 2 km and 2 m, respectively. To avoid thermal lag effects, salinity data were corrected using Garau et al.'s (2011) algorithm. Full details of the glider mission, of the formation and early life of Poseidon, and its detailed vertical structure are reported in Meunier et al. (2018). Geostrophic velocity u_g was computed using the observed density field and referenced using the depth averaged currents measured by the glider's drift between two surfacing events, following Rudnick et al. (2015). Because ITEs are embedded within the larger-scale velocity field of the LCE, an average advection velocity was subtracted from the geostrophic velocity to isolate the ITE's currents, following Bosse et al. (2015). The cyclogeostrophic velocity were then computed from the geostrophic velocity, following Elliott and Sanford (1986) and Bosse et al. (2015):

$$u(r,z) = \frac{rf}{2}\left(-1 \pm \sqrt{1 - 4\frac{u_g}{r}}\right), \tag{1}$$

where r and z are the radial and vertical coordinates, respectively. Relative vorticity was then computed from the cyclogeostrophic velocity:

$$\xi(r,z) = \frac{1}{r}\partial_r(ru(r,z)). \tag{2}$$

Because the glider section is two-dimensional and ITEs do not have any surface signature that could be tracked using altimetry, an uncertainty on the radial coordinate is inevitable. In the case of a circular eddy, the true path of the glider might be on a chord, shifted from the eddy center by a certain distance δ, and the along-track coordinate is not r but $\lambda = \sqrt{r^2 - \delta^2}$. This will introduce an error on any tracer distribution, which will be amplified when computing radial derivatives or any operation depending on the radius, as is done when computing velocity and relative vorticity. Unfortunately, in the absence of any supplementary data source, the only way to estimate the velocity and vorticity here is to assume that the glider directly sliced through the eddy's center, introducing an error that cannot be directly estimated from the data, and the reader should keep in mind that the ITE's properties discussed in the present paper rely on this assumption. An analytical quantitative study of the impact of a shift in the glider's trajectory on the important variables computed in this paper was performed using an idealized vortex lens profile and is available in Appendix A. It shows that, in the case of an anticyclonic lens, velocity and relative vorticity will be underestimated. The shift obviously also reduces the apparent size of the surveyed structures: An eddy with a radius R will appear to be $L = \sqrt{(R^2 - \delta^2)}$. Both effects feed through the Rossby and Burger numbers, which may be underestimated and overestimated, respectively.

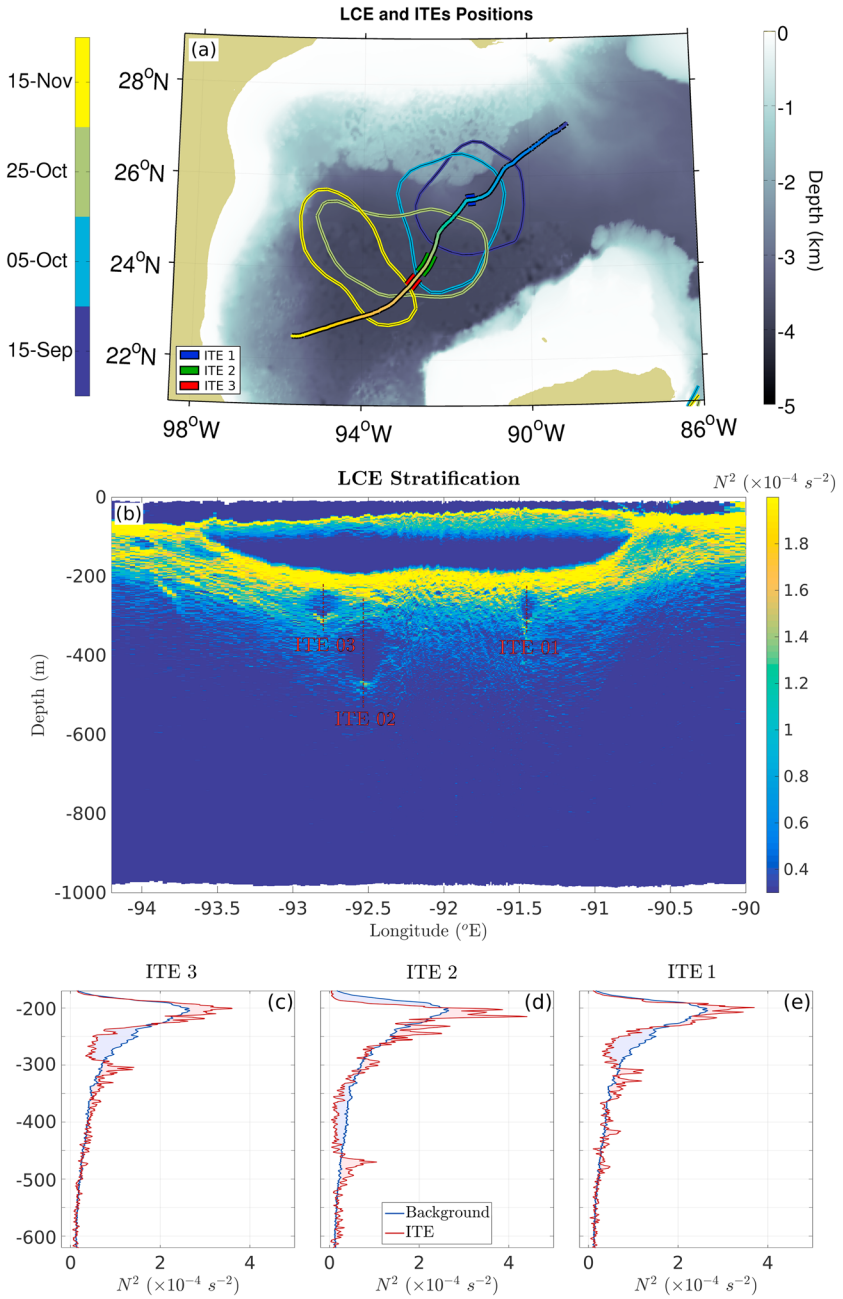

Figure 1. (a) Map of the glider transect through the central GoM. Loop current eddy (LCE) Poseidon is materialized by the 0.7-m contours of absolute dynamic topography. Time is color coded in both the ADT contours and the glider's track. ITEs 1, 2, and 3's positions are materialized by blue, green, and red segments, respectively. (b) Vertical section of squared Brunt Väisälä (N^2) across LCE Poseidon. ITEs centers are marked with a red vertical line. They are obvious as bubbles of weak stratification embedded within the LCE's well stratified lower pycnocline below the eddy core. (c–e) Vertical profiles of N^2 through the centers of ITEs 1, 2, and 3 (materialized by a red line in panel b) compared with an average profile within the LCE core (blue line). While ITEs cores are obvious as negative anomalies of N^2 (blue shaded areas), lobes of positive anomalies (red shaded areas) surround the ITEs cores in each case. ITE = intrathermocline eddy.

The squared Brunt-Väisälä frequency $N^2 = -g\partial_z\sigma/\sigma$ (where σ is potential density), and the Ertel PV and PV anomaly (PVA) are particularly suited quantities to identify and describe ITEs (D'Asaro, 1988b; McWilliams, 1985; Thomas, 2008). PVA is the difference between local PV (q) and a reference ambient PV ($\overline{Q}_P$), which is chosen here to be the average PV within the LCE's central part (core) at the ITE's mean depth.

Similarly, σ and N^2 are decomposed as the sum of a mean part ($\overline{\sigma}_P(z)$ and $\overline{N}^2_P(z)$) corresponding to the average LCE core's conditions and a perturbation part ($\sigma'(r,z)$ and $N^{2'}(r,z)$) corresponding to the ITE's local anomaly.

ITEs were observed to be far from the LCE's frontal region where the horizontal density gradients and the vertical velocity shear are strong (Meunier et al., 2018); hence, horizontal components of relative vorticity can be neglected. Computing relative vorticity of large and quickly evolving mesoscale eddies such as LCEs is challenging, especially when sampled with a slow vehicle, because of the difficulty to identify properly their rotation axis. The ambient relative vorticity ξ_P corresponding to LCE Poseidon is evaluated using the scaling $\xi_P \approx 2fRo_P$, where $Ro_P = U_p/fR_P$ is the LCE's Rossby number, U_p is the LCE's peak velocity averaged over the depth of the ITEs, and R_p is the approximate LCE's radius. Under these assumptions, the local and ambient PV respectively read

$$q = \frac{(f+\xi)}{g}N^2, \tag{3}$$

where ξ is the local vertical component of the relative vorticity and

$$\overline{Q}_P = \frac{f(1+2Ro_P)}{g}\overline{N}^2_P. \tag{4}$$

The nondimensional form of PVA, $q^* = \frac{q-\overline{Q}_P}{\overline{Q}_P}$, can be expressed as

$$q^* = N^{*2} + \xi^* + \xi^* N^{*2}, \tag{5}$$

where $\xi^* = \xi/f(1+2Ro_P)$ is the nondimensional vertical components of the ITE's relative vorticity and $N^{*2} = N'^2/\overline{N}^2_P$ is the nondimensional squared Brunt-Väisälä frequency anomaly corresponding to the vortex stretching term.

3. Results

The stratification structure of LCE Poseidon is shown on the Brunt-Väisälä section of Figure 1b: The LCE is obvious as a large body of nearly homogeneous water between 50 and 200 m, splitting the pycnocline and deflecting it downward below the eddy. The ITEs were surveyed between 3 and 5 October (ITE 1), between 23 and 25 October (ITE 2), and between 25 and 27 October (ITE 3). They are evident as lenses of well-mixed water (weak N^2) embedded in the more stratified LCE main pycnocline. They are centered at 92.8 (ITE 3), 92.5 (ITE 2), and 91.45°W (ITE 1) at the depths of 280, 395, and 270 m, have radii of 19, 32, and 25 km, respectively. Vertical profiles of N^2 through the ITE's centers are compared to the average LCE core's profile in Figures 1c–e. They reveal the presence of stratification maxima above and below the negative stratification anomalies; while isopycnals are stretched within the ITEs cores, they are squeezed above and below. Considering the positive N^2 anomaly lobes as part of the ITEs, their total thickness respectively reach 160, 250, and 150 m, while the negative N^2 anomaly cores alone are 60, 150, and 65 m thick.

Cyclogeostrophic velocity associated with the isopycnal spreading (Figure 2) shows typical vortex lens characteristics in ITEs 1 and 2, including closed isotachs around the velocity maximum, and both azimuthal and vertical symmetry of the velocity field. ITE 3's isotachs are not strictly closed and do not show the same symmetry. ITEs 1, 2, and 3 have cyclogeostrophic velocity maxima of 0.26, 0.23, and 0.16 m/s, respectively.

Relative vorticity associated with the anticyclonic circulation ranges between −0.85 and −0.46 f. For comparison, the LCE's relative vorticity at the depth of 250 m computed using equation (4) ranges between −0.03 and −0.06 f, considering average azimuthal velocity of 0.25 to 0.5 m/s and a radius of 150 km (Meunier et al., 2018). ITEs relative vorticity is 8 to 28 times larger, suggesting that ITEs vorticity is little affected by the LCE.

The combination of the intense anticyclonic vorticity and the negative stratification anomaly yields an anomalously low PV (equation (3)) in all three ITEs (Figures 3a–c). Analysis of the PVA structure (Figure 3d) shows that the cores are characterized by patches of negative PVA surrounded above and below by thin lobes of positive PVA. Analysis of the terms of equation (5) shows a moderate dominance of the vortex stretching term N^{*2} over relative vorticity ξ^* in the central core of ITE 3, an opposite situation in ITE 1, and an equal contribution in ITE 2. Defining the Burger number as the ratio of relative vorticity to vortex stretching averaged over the vortex core, values of 1.24, 1.04, and 0.73 were found for ITEs 1, 2, and 3 respectively. Contrary to N^{*2},

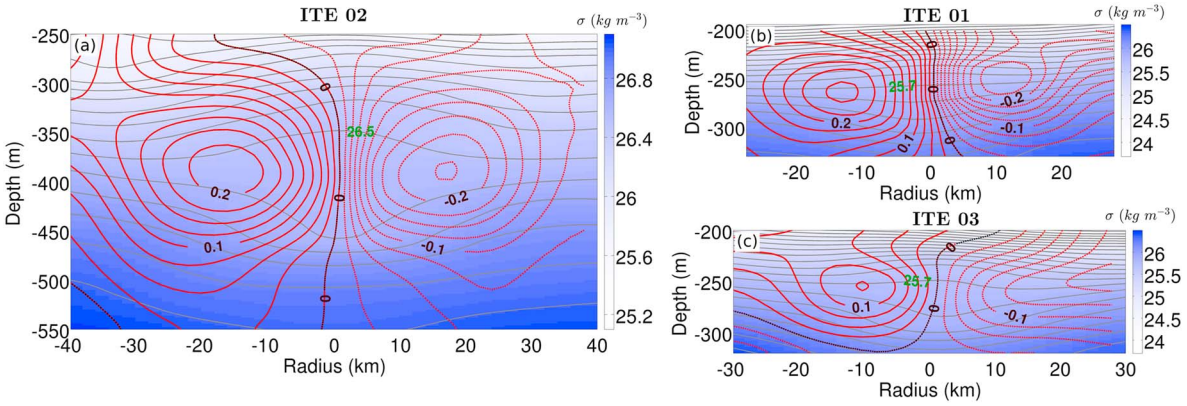

Figure 2. Cyclogeostrophic velocity (red contours) superimposed on potential density maps (color) of the three intrathermocline eddies (ITEs). For clarity, only the mid-depth isopycnals are labeled. The contour spacing is 0.1 kg/m^{-3}. The velocity contour spacing is of 0.025 m/s.

ξ^* is negative all over the ITE's thickness, so that the positive PVA lobes are more driven by vortex stretching. Since ξ^* and N^{*2} are of the same sign within the ITEs cores, where stratification anomaly is negative, the nonlinear term $\xi^* N^{*2}$ is positive, and tends to diminish PVA intensity. The opposite situation is observed in the lobes, where ξ^* and N^{*2} have opposite signs.

The thermohaline structure of the ITEs is described and compared with the surrounding LCE water mass in the T-S diagram of Figure 4. The blue, green, and red dotted lines represent vertical profiles through the cores of ITEs 1, 2, and 3, respectively, the black dotted line represents the average of all LCE profiles between 91.8 and 92.3°W and the gray line represents the Common Gulf Water (CGW) measured far outside the LCE. The shallower ITEs 1 and 3 are centered in the lower part of the T-S curvature associated with the SUW salinity maximum. A detailed look at the T-S diagram (Figure 4b) reveals a straight line T-S distribution

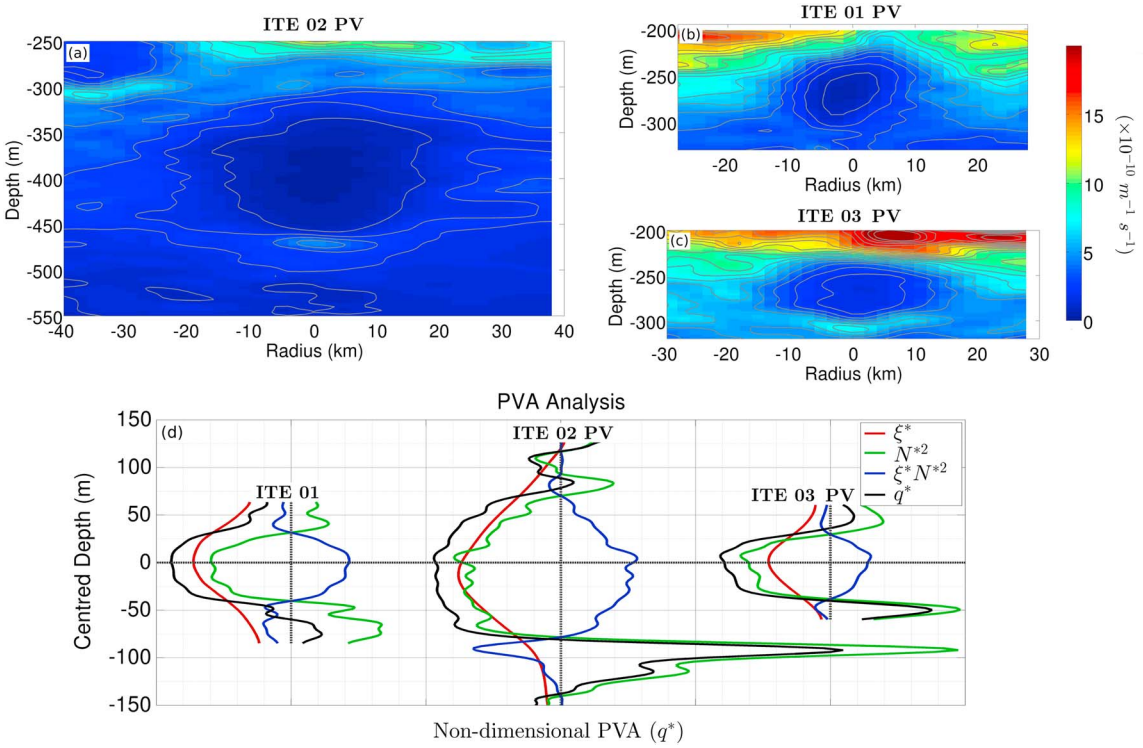

Figure 3. (a–c) Vertical sections of PV for each intrathermocline eddy (ITE). (d) Analysis of the contribution of each term in the nondimensional potential vorticity anomaly (PVA). The red lines represent relative vorticity ξ^*, the green line is the vortex stretching term N^{*2}, the blue line is the product of both ($\xi^* N^{*2}$), and the black line is the total nondimensional PVA. The Tilting term is two orders of magnitudes smaller and is not plotted.

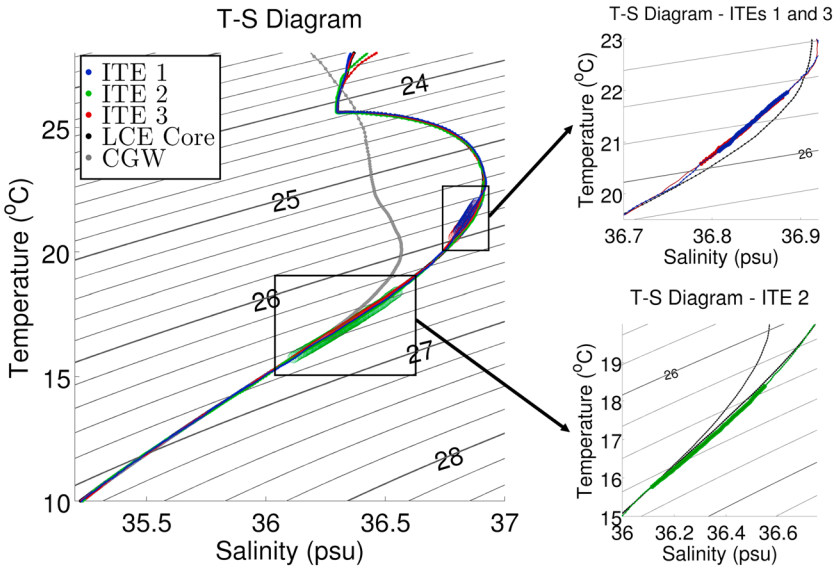

Figure 4. (a) T-S diagram of an average loop current eddy (LCE) vertical profile (black dotted line), a Common Gulf Water (CGW) profile (gray dotted line), and the three profiles through the cores of ITEs 1, 2, and 3 (red, green, and blue dotted lines, respectively). (b) Zoom on ITEs 1 and 3. (c) Zoom on ITE 2. In each panel, the ITE's localization is materialized by thicker dots.

within ITEs 1 and 3 between the 25.6- and 26.1-kg/m^3 isopycnals, literally taking a shortcut through the curved LCE T-S distribution, suggesting that diapycnal mixing might have occurred. Oppositely, the T-S signature of ITE 2 is not discernible (Figure 4c), presumably because salinity decreases nearly linearly with temperature within the LCE at this depth. The absence of any obvious difference between ITEs and average LCE's water masses, apart from a local mixing evidence, contrasts with most observed ITEs in the literature, which usually carry strong thermohaline signatures.

ITEs 1 and 3 have similar T-S signatures and sizes and could therefore be suspected to be one single structure advected around the LCE during the glider's transect and surveyed twice. However, their PV minimum considerably differ ($0.5 \times 10^{-10} \cdot m^{-1} \cdot s^{-1}$ and $1.5 \times 10^{-10} \cdot m^{-1} \cdot s^{-1}$, respectively). As PV is a conservative tracer, this difference supports the idea that they are two different structures. The uncertainty on relative vorticity inherent to the blind glider trajectory discussed in section 2 and in Appendix A could not explain such a difference of magnitude.

4. Discussion and Conclusion

Although ITEs were intensively observed and studied throughout the ocean, those reported in the present paper show three original or rare characteristics: They are the first ITEs ever observed within the GoM, they are embedded within a large anticyclonic vortex ring, and their thermohaline properties do not contrast sharply with the surrounding LCE water. The T-S distribution considerably constrains the possible formation mechanisms: While ITE's subduction at the sharp frontal edges of LCEs may occur, especially when favored by intermittent strong northerly winds during autumn and winter over the GoM, this process is unlikely to have formed the observed ITEs because their thermohaline signature would be that of the adjacent water mass, namely, CGW (Figure 4).

Frictional processes, such as PV reduction by boundary torques, were also shown to be an efficient ITE formation mechanism (D'Asaro, 1988b). Intense negative vorticity is generated within a frictional boundary layer when an undercurrent flows with a topographic boundary on its right; if the topography sharply turns to the right at some point (as in the case of a cape or a promontory), the sheared current separates and the anticyclonic shear layer evolves as a series of anticyclonic ITEs. However, the possibility for a boundary torque to generate ITEs from the LCE current within the GoM seems difficult. The only topographic interactions that LCEs may experience would be with the GoM's northern and southern shelves and slope. LCEs are anticyclonic, so that friction against these boundaries would result in the formation of a cyclonic shear layer,

which can obviously not account for the observed anticyclonic ITEs. Small satellite cyclones were observed to form around LCEs and travel with them (Chérubin et al., 2005; Rudnick et al., 2015). Frictional torque of the latter against the GoM boundaries would indeed form anticyclonic shear layers that could evolve into anticyclonic ITEs, but their thermohaline properties would be closer to CGW than SUW (Rudnick et al., 2015), and they would likely form at the periphery of the LCE, not near their centers as observed here.

The stratification breakdown and low PV found within all three ITEs, the lack of contrast between the water they carry and LCE water, and the well-defined mixing line observed within ITEs 1 and 3 suggest that they might form through intense mixing, followed by Rossby adjustment, as proposed by McWilliams (1985): Strong diapycnal mixing would homogenize quickly a patch of water, setting up an azimuthal current to reach the geostrophic equilibrium, hence spinning up a balanced anticyclonic circulation.

The mixing and adjustment theory requires to identify a possible source of diapycnal mixing that would be able to homogenize such thick bodies of water. Bottom friction of a strong current against rough topography could lead to intense mixing, either through drag in a frictional bottom boundary layer (Marshall & Naveira Garabato, 2008; McWilliams, 1985) or by the generation of breaking internal wave, as discussed by Marshall and Naveira Garabato (2008) and Lelong and Sundermeyer (2005). Because the first process would be confined within a bottom boundary layer, it requires to identify a sufficiently shallow zone (less than 500 m depth for ITE 2 and 350 m for ITEs 1 and 3) over which the intense velocity annulus of LCE Poseidon have passed. A joint examination of altimetry and bathymetry data (not shown) shows that such an event only happened briefly over the tip of the Campeche Bank in May 2016, soon after Poseidon's detachment. Oppositely, internal waves can propagate vertically and could therefore be generated well below the ITEs depth, which would not constrain as much the water depth when searching for a potential generation site.

The possibility of ITE generation prior to LCE formation cannot be ruled out. The loop current is an intense current (over 1.5 m/s; Oey et al., 2005), flowing along the Yucatan's east coast over an irregular shelf and slope, including impinging of the current against the coast in the Caribbean sea prior to entering the Gulf, which could be sources of spatially irregular mixing. ITEs would then be advected northward and trapped within detaching LCEs.

As the ITEs observed in the GoM share the thermohaline properties of the much larger LCE in which they were embedded at the time of the glider survey, their contribution in the advection and diffusion of heat and salt in the basin may seem secondary at first sight. The significance of their impact likely depend on the number of ITEs travelling with the LCE and their ability to escape from it. If they remain trapped, their fate is to reach the Western GoM and dissipate in the so-called eddy graveyard along with the large LCE. If they leave the LCE and are entrained by the surrounding mesoscale turbulence, they could carry their thermohaline content to areas of the GoM that are not affected by LCEs. The observation of three ITEs in a single transect suggests that these structures might be abundant hence have an important impact on the redistribution of SUW throughout the gulf.

So far, little is known about these structures, from their generation process to their fate and possible impacts. Upcoming ship surveys as well as repeated glider missions in the GoM as part of the CIGoM project will help to a better understanding of these ITEs.

Appendix A: Estimating the Error Induced by a Shift Between a Glider's Trajectory and the Center of an Idealized Vortex Lens

To infer the impact of the error associated with a glider trajectory shifted from the center of the eddy, an analytical model was built, fitting the ITEs velocity field to a Cauchy-Lorentz distribution stream function. The latter was shown to be suited to match vortex lenses (Hua et al., 2013; Meunier et al., 2015) and is defined as follows:

$$\psi(r,z) = \psi_0(1+\Gamma^2+\Gamma^4)^{-1}, \tag{A1}$$

$$\Gamma = \sqrt{\frac{r^2}{R^2}+\frac{z^2}{H^2}}, \tag{A2}$$

where H and R are the ITE's thickness and radius, respectively. The close fit between the analytical and ITE 2's velocity fields is obvious in Figures A1a–c. Synthetic "Glider-measured" density anomaly, cyclogeostrophic

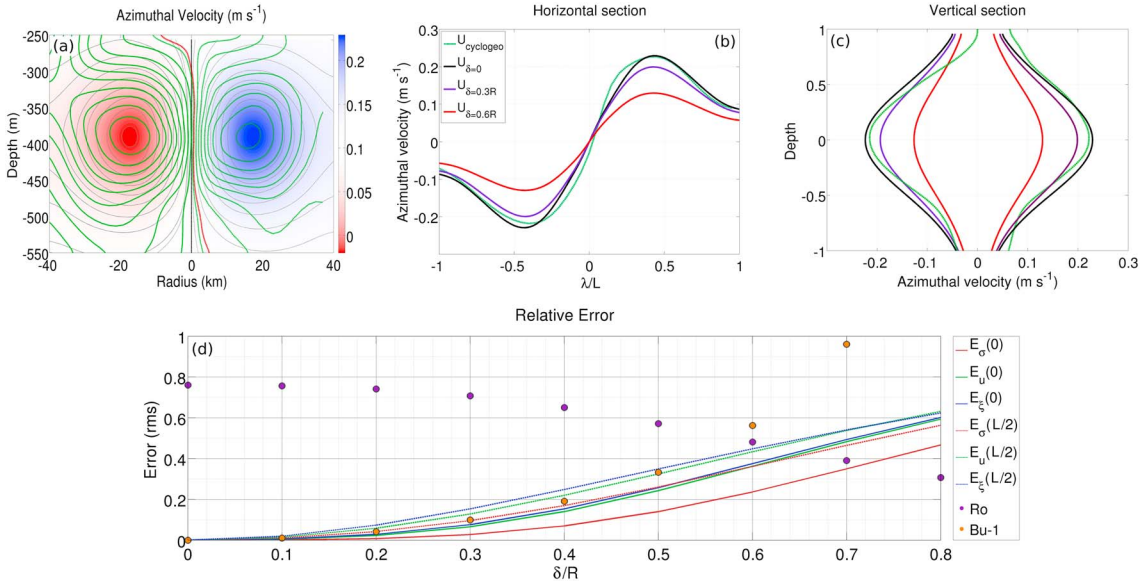

Figure A1. (a) Cauchy-Lorentz fit of ITE 2's velocity field (color). The observed cyclogeostrophic velocity ($U_{cyclogeo}$) is plotted as green contours. The contour interval is of 0.025 m/s. (b) Horizontal profile of the azimuthal velocity: The green line is the cyclogeostrophic velocity inferred from the glider data; the black, purple, and red lines are the Cauchy-Lorentz velocity computed in λ coordinates for $\delta = 0$, 0.3, and 0.6 R, respectively. (c) Vertical profile of the azimuthal velocity: The same color code as in (b) is used. Depth was nondimensionalized by the ITE's thickness. (d) Relative errors on σ (red lines), u (green lines), and ξ (blue line) at $\lambda = 0$ (continuous lines), and $\lambda = L/2$ (dotted lines), as a function of δ. Rossby (purple dots) and Burger (orange dots) numbers are also plotted against δ.

velocity, and relative vorticity $[\tilde{\sigma}, \tilde{u}, \tilde{\xi}](\lambda, z)$ were computed by defining a trajectory along a chord L of the circular eddy, shifted from the center by a distance δ. The along-chord coordinate, λ, is defined as $\lambda = \sqrt{r^2 - \delta^2}$. Relative errors on density anomaly, cyclogeostrophic velocity, and relative vorticity are defined as follows:

$$\epsilon_{[\sigma,u,\xi]} = \left\| \frac{[\tilde{\sigma}, \tilde{u}, \tilde{\xi}](\lambda, z) - [\sigma, u, \xi](r, z)}{[\sigma, u, \xi](r, z)} \right\|. \tag{A3}$$

Radial and vertical velocity profiles computed in λ coordinates are shown for different values of δ in Figures A1b and A1c, respectively. Relative errors on σ, u, and ξ at $\lambda = 0$ and $\lambda = L/2$ are shown in Figure A1d. Because they depend on radial derivatives, relative errors on ξ and u are larger than on σ. Errors also appear to be stronger near the velocity maximum at $\lambda = L/2$ than near the eddy center. However, for a shift of $\delta = 0.3R$, relative errors remain moderate (under 0.1 for σ, 0.12 for u, and 0.16 for ξ), and only for $\delta > 0.7$ does the error on relative vorticity within the eddy center reach 0.5. A Rossby number of 0.76 in radial coordinate will appear to be 0.7 and 0.38 in λ coordinate for $\delta = 0.3$ and $\delta = 0.7R$, respectively. Similarly, a Burger number unity in radial coordinate will increase to 1.1 and 1.9 in λ coordinate for $D = 0.3$ and 0.7, respectively. In the case of a glider surveying a 30-km-radius ITE and missing its center by about 10 km, the relative errors would remain moderate.

Acknowledgments
The glider mission was performed by the Grupo de Monitoreo Oceanografo con Gliders (CICESE, UNAM, CIDESI,CICATA). Research funded by the National Council of Science and Technology of Mexico - Mexican Ministry of Energy - Hydrocarbon Trust, project 201441. This is a contribution of the Gulf of Mexico Research Consortium (CIGoM). T. Meunier was funded by a postdoctoral scholarship from CICESE, funded via a grant of the National Council of Science and Technology of Mexico-Secretariat of Energy-Hidrocarbons Trust, project 201441. The altimeter products were produced by Ssalto/Duacs and distributed by Aviso, with support from Cnes (http://www.aviso.altimetry.fr/duacs/). The authors are grateful to Pr. Des Barton for the valuable discussions and suggestions, as well as two anonymous reviewers whose constructive criticism helped to improve this manuscript. T. Meunier would like to dedicate this work to the memory of his godfather and colleague Jean-Pierre Bergeron, who devoted his life to the understanding of the ocean. The raw data set used in this study can be visualized on the GMOG's webpage: https://gliders.cicese.mx/. The full data can be distributed upon request to T. Meunier for reviewing purpose and will be publicly accessible on the GMOG's webpage in January 2020.

References

Armi, L., Hebert, D., Oakey, N., Price, J. F., Richardson, P. L., Thomas Rossby, H., & Ruddick, B. (1989). Two years in the life of a Mediterranean salt lens. *Journal of Physical Oceanography*, *19*, 354–370. https://doi.org/10.1175/1520-0485(1989)019<0354:TYITLO>2.0.CO;2

Baird, M. E., & Ridgway, K. R. (2012). The southward transport of sub-mesoscale lenses of Bass Strait Water in the centre of anti-cyclonic mesoscale eddies. *Geophysical Research Letters*, *39*, L02603. https://doi.org/10.1029/2011GL050643

Bosse, A., Testor, P., Mortier, L., Prieur, L., Taillandier, V., d'Ortenzio, F., & Coppola, L. (2015). Spreading of Levantine Intermediate Waters by submesoscale coherent vortices in the northwestern Mediterranean Sea as observed with gliders. *Journal of Geophysical Research: Oceans*, *120*, 1599–1622. https://doi.org/10.1002/2014JC010263

Brenner, S. (1989). Structure and evolution of warm core eddies in the eastern Mediterranean Levantine Basin. *Journal of Geophysical Research*, *94*(C9), 12,593–12,602. https://doi.org/10.1029/JC094iC09p12593

Chérubin, L. M., Morel, Y., & Chassignet, E. P. (2005). Loop current ring shedding: The formation of cyclones and the effect of topography. *Journal of Physical Oceanography*, *36*(4), 569–591.

Collins, C. A., Margolina, T., Rago, T. A., & Ivanov, L. (2013). Looping RAFOS floats in the California Current system. *Deep Sea Research Part II: Topical Studies in Oceanography*, *85*, 42–61. https://doi.org/10.1016/j.dsr2.2012.07.027

D'Asaro, E. A (1988a). Observations of small eddies in the Beaufort Sea. *Journal of Geophysical Research*, *93*(C6), 6669–6684. https://doi.org/10.1029/JC093iC06p06669

D'Asaro, E. A (1988b). Generation of submesoscale vortices: A new mechanism. *Journal of Geophysical Research*, *93*(C6), 6685–6693. https://doi.org/10.1029/JC093iC06p06685

Damien, P., Bosse, A., Testor, P., Marsaleix, P., & Estournel, C. (2017). Modeling postconvective submesoscale coherent vortices in the northwestern Mediterranean Sea, *122*, 9937–9961. https://doi.org/10.1002/2016JC012114

Dugan, J. P., Mied, R. P., Mignerey, P. C., & Schuetz, A. F. (1982). Compact, intrathermocline eddies in the Sargasso Sea. *Journal of Geophysical Research*, *87*(C1), 385–393. https://doi.org/10.1029/JC087iC01p00385

Elliott, B. A. (1982). Anticyclonic rings in the Gulf of Mexico. *Journal of Physical Oceanography*, *12*, 1292–1309. https://doi.org/10.1175/1520-0485(1982)012<1292:ARITGO>2.0.CO;2

Elliott, B. A., & Sanford, T. B. (1986). The subthermocline lens D1. Part II: Kinematics and dynamics. *Journal of Physical Oceanography*, *16*, 549–561. https://doi.org/10.1175/1520-0485(1986)016<0549:TSLDPI>2.0.CO;2

Garau, B., Ruiz, S., Zhang, W. G., Pascual, A., Heslop, E., Kerfoot, J., & Tintoré, J. (2011). Thermal lag correction on Slocum CTD Glider data. *Journal of Atmospheric and Oceanic Technology*, *28*, 1065–1071. https://doi.org/10.1175/JTECH-D-10-05030.1

Glenn, S. M., & Ebbesmeyer, C. C. (1993). Drifting buoy observations of a loop current anticyclonic eddy. *Journal of Geophysical Research*, *98*(C11), 20,105–20,119. https://doi.org/10.1029/93JC02078

Gordon, A. L., Giulivi, C. F., Lee, C. M., Furey, H. H., Bower, A., & Talley, L. (2002). Japan/East Sea intrathermocline eddies. *Journal of Physical Oceanography*, *32*, 1960–1974. https://doi.org/10.1175/1520-0485(2002)032<1960:JESIE>2.0.CO;2

Gordon, A. L., Shroyer, E., & Murty, V. S. N. (2017). An intrathermocline eddy and a tropical cyclone in the Bay of Bengal. *Scientific Reports*, *7*, 46218. https://doi.org/10.1038/srep46218

Hallock, Z. R., Teague, W. J., & Broome, R. D. (1981). A deep, thick, isopycnal layer within an anticyclonic eddy. *Journal of Physical Oceanography*, *11*, 1674–1676. https://doi.org/10.1175/1520-0485(1981)011<1674:ADTILW>2.0.CO;2

Hebert, D. (1988). Mediterranean salt lenses. *Elsevier Oceanography Series*, *46*, 229–237.

Hernández-Guerra, A., & Joyce, T. M. (2000). Water masses and circulation in the surface layers of the Caribbean at 66°W. *Geophysical Research Letters*, *27*(21), 3497–3500. https://doi.org/10.1029/1999GL011230

Hua, B. L., Ménesguen, C., Le Gentil, S., Schopp, R., Marsset, B., & Aiki, H. (2013). Layering and turbulence surrounding an anticyclonic oceanic vortex: In situ observations and quasi-geostrophic numerical simulations. *Journal of Fluid Mechanics*, *731*, 418–442. https://doi.org/10.1017/jfm.2013.369

Ichiye, T. (1959). Circulation and water-mass distribution in the gulf of mexico. *Journal of Geophysical Research*, *64*(8), 1109–1110.

Johnson, D. R., Thompson, J. D., & Hawkins, J. D. (1992). Circulation in the Gulf of Mexico from Geosat altimetry during 1985-1986. *Journal of Geophysical Research*, *97*(C2), 2201–2214. https://doi.org/10.1029/90JC02400

Jungclaus, J. H. (1999). A three-dimensional simulation of the formation of anticyclonic lenses (meddies) by the instability of an intermediate depth boundary current. *Journal of Physical Oceanography*, *29*, 1579–1598. https://doi.org/10.1175/1520-0485(1999)029<1579:ATDSOT>2.0.CO;2

Kostianoy, A. G., & Belkin, I. M. (1989). A survey of observations on emtrathermocline eddies in the world ocean. *Elsevier Oceanography Series*, *50*, 821–841.

L'Hégaret, P., Carton, X., Louazel, S., & Boutin, G. (2016). Mesoscale eddies and submesoscale structures of Persian Gulf Water off the Omani coast in spring 2011. *Ocean Science*, *12*, 687–701. https://doi.org/10.5194/os-12-687-2016

Lelong, M.-P., & Sundermeyer, M. A. (2005). Geostrophic adjustment of an isolated diapycnal mixing event and its implications for small-scale lateral dispersion. *Journal of Physical Oceanography*, *35*, 2352. https://doi.org/10.1175/JPO2835.1

Lilly, J. M., & Rhines, P. B. (2002). Coherent eddies in the Labrador Sea observed from a mooring. *Journal of Physical Oceanography*, *32*, 585–598. https://doi.org/10.1175/1520-0485(2002)032<0585:CEITLS>2.0.CO;2

Marshall, D. P., & Naveira Garabato, A. C. (2008). A conjecture on the role of bottom-enhanced diapycnal mixing in the parameterization of geostrophic eddies. *Journal of Physical Oceanography*, *38*, 1607–1613. https://doi.org/10.1175/2007JPO3619.1

McWilliams, J. C (1985). Submesoscale, coherent vortices in the ocean. *Reviews of Geophysics*, *23*(2), 165–182. https://doi.org/10.1029/RG023i002p00165

McWilliams, J. C. (1988). Vortex generation through balanced adjustment. *Journal of Physical Oceanography*, *18*, 1178–1192. https://doi.org/10.1175/1520-0485(1988)018<1178:VGTBA>2.0.CO;2

Meunier, T., Ménesguen, C., Schopp, R., & Le Gentil, S. (2015). Tracer stirring around a meddy: The formation of layering. *Journal of Physical Oceanography*, *45*, 407–423. https://doi.org/10.1175/JPO-D-14-0061.1

Meunier, T., Pallás-Sanz, E., Tenreiro, M., Portela Rodriguez, E., Ochoa, J., Ruiz-Angulo, A., & Cusí, S. (2018). The vertical structure of a loop current eddy. *Journal of Geophysical Research: Oceans*, *123*. https://doi.org/10.1029/2018JC013801

Molemaker, M. J., McWilliams, J. C., & Dewar, W. K. (2015). Submesoscale instability and generation of mesoscale anticyclones near a separation of the California undercurrent. *Journal of Physical Oceanography*, *45*, 613–629. https://doi.org/10.1175/JPO-D-13-0225.1

Oey, L.-Y., Jr., Ezer, T., & Lee, H.-C. (2005). Loop current, rings and related circulation in the Gulf of Mexico: A review of numerical models and future challenges. *Washington DC American Geophysical Union Geophysical Monograph Series*, *161*, 31–56. https://doi.org/10.1029/161GM04

Ou, H.-W., & Gordon, A. (2002). Subduction along a midocean front and the generation of intrathermocline eddies: A theoretical study. *Journal of Physical Oceanography*, *32*, 1975–1986. https://doi.org/10.1175/1520-0485(2002)032<1975:SAAMFA>2.0.CO;2

Pingree, R. D., & Le Cann, B. (1992). Anticyclonic eddy X91 in the southern Bay of Biscay, May 1991 to February 1992. *Journal of Geophysical Research*, *97*(C9), 14,353–14,367. https://doi.org/10.1029/92JC01181

Rudnick, D. L., Gopalakrishnan, G., & Cornuelle, B. D. (2015). Cyclonic eddies in the Gulf of Mexico: Observations by underwater gliders and simulations by numerical model. *Journal of Physical Oceanography*, *45*, 313–326. https://doi.org/10.1175/JPO-D-14-0138.1

Shapiro, G. I., & Meschanov, S. L. (1991). Distribution and spreading of Red Sea Water and salt lens formation in the northwest Indian Ocean. *Deep Sea Research A*, *38*, 21–34. https://doi.org/10.1016/0198-0149(91) 90052-H

Stuart, G. A., Sundermeyer, M. A., & Hebert, D. (2011). On the geostrophic adjustment of an isolated lens: Dependence on burger number and initial geometry*. *Journal of Physical Oceanography*, *41*, 725–741. https://doi.org/10.1175/2010JPO4476.1

Testor, P., & Gascard, J.-C. (2003). Large-scale spreading of deep waters in the western Mediterranean Sea by submesoscale coherent eddies. *Journal of Physical Oceanography*, *33*, 75–87. https://doi.org/10.1175/1520-0485(2003)033<0075:LSSODW>2.0.CO;2

Thomas, L. N. (2008). Formation of intrathermocline eddies at ocean fronts by wind-driven destruction of potential vorticity. *Dynamics of Atmospheres and Oceans*, *45*, 252–273. https://doi.org/10.1016/j.dynatmoce.2008.02.002

Thomsen, S., Kanzow, T., Krahmann, G., Greatbatch, R. J., Dengler, M., & Lavik, G. (2016). The formation of a subsurface anticyclonic eddy in the Peru-Chile undercurrent and its impact on the near-coastal salinity, oxygen, and nutrient distributions. *Journal of Geophysical Research: Oceans*, *121*, 476–501. https://doi.org/10.1002/2015JC010878

Vukovich, F. M. (1995). An updated evaluation of the loop current's eddy-shedding frequency. *Journal of Geophysical Research*, *100*, 8655–8659. https://doi.org/10.1029/95JC00141

Wüst, G. (1964). *Stratification and circulation in the Antillean-Caribbean basins* (Vol. 1). New York: Columbia University Press.